Nanoscale

PAPER

View Article Online
View Journal | View Issue

Cite this: *Nanoscale*, 2022, **14**, 9877

Metamagnetic transition and a loss of magnetic hysteresis caused by electron trapping in monolayers of single-molecule magnet $Tb_2@C_{79}N$†

Emmanouil Koutsouflakis,[a] Denis Krylov,‡[a] Nicolas Bachellier,[b] Daria Sostina,§[b] Vasilii Dubrovin,[a] Fupin Liu,[a] Lukas Spree,[a] Georgios Velkos,[a] Sebastian Schimmel,¶[a] Yaofeng Wang,[a] Bernd Büchner,[a] Rasmus Westerström,[c,d] Claudiu Bulbucan,[c,d] Kyle Kirkpatrick,[e] Matthias Muntwiler,[b] Jan Dreiser,[b] Thomas Greber,[b,f] Stas M. Avdoshenko,[a] Harry Dorn[e] and Alexey A. Popov*[a]

Realization of stable spin states in surface-supported magnetic molecules is crucial for their applications in molecular spintronics, memory storage or quantum information processing. In this work, we studied the surface magnetism of dimetallo-azafullerene $Tb_2@C_{79}N$, showing a broad magnetic hysteresis in a bulk form. Surprisingly, monolayers of $Tb_2@C_{79}N$ exhibited a completely different behavior, with the prevalence of a ground state with antiferromagnetic coupling at low magnetic field and a metamagnetic transition in the magnetic field of 2.5–4 T. Monolayers of $Tb_2@C_{79}N$ were deposited onto Cu(111) and Au (111) by evaporation in ultra-high vacuum conditions, and their topography and electronic structure were characterized by scanning tunneling microscopy and spectroscopy (STM/STS). X-ray photoelectron spectroscopy (XPS), in combination with DFT studies, revealed that the nitrogen atom of the azafullerene cage tends to avoid metallic surfaces. Magnetic properties of the (sub)monolayers were then studied by X-ray magnetic circular dichroism (XMCD) at the Tb-$M_{4,5}$ absorption edge. While in bulk powder samples $Tb_2@C_{79}N$ behaves as a single-molecule magnet with ferromagnetically coupled magnetic moments and blocking of magnetization at 28 K, its monolayers exhibited a different ground state with antiferromagnetic coupling of Tb magnetic moments. To understand if this unexpected behavior is caused by a strong hybridization of fullerenes with metallic substrates, XMCD measurements were also performed for $Tb_2@C_{79}N$ adsorbed on h-BN|Rh(111) and MgO|Ag(100). The co-existence of two forms of $Tb_2@C_{79}N$ was found on these substrates as well, but magnetization curves showed narrow magnetic hysteresis detectable up to 25 K. The non-magnetic state of $Tb_2@C_{79}N$ in monolayers is assigned to anionic $Tb_2@C_{79}N^-$ species with doubly-occupied Tb–Tb bonding orbital and antiferromagnetic coupling of the Tb moments. A charge transfer from the substrate or trapping of secondary electrons are discussed as a plausible origin of these species.

Received 27th December 2021,
Accepted 28th June 2022

DOI: 10.1039/d1nr08475e

rsc.li/nanoscale

[a]*Leibniz Institute for Solid State and Materials Research (IFW Dresden), Helmholtzstraße 20, 01069 Dresden, Germany. E-mail: a.popov@ifw-dresden.de*
[b]*Swiss Light Source, Paul Scherrer Institute, CH-5232 Villigen PSI, Switzerland*
[c]*The Division of Synchrotron Radiation Research, Lund University, SE-22100 Lund, Sweden*
[d]*NanoLund, Lund University, Box 118, 22100 Lund, Sweden*
[e]*Department of Chemistry, Virginia Polytechnic Institute and State University, Blacksburg, Virginia 24061, USA*
[f]*Physik-Institut der Universität Zürich, Winterthurerstr. 190, CH-8057 Zürich, Switzerland*

†Electronic supplementary information (ESI) available. See DOI: https://doi.org/10.1039/d1nr08475e

‡Current address: Quantum Nanoscience, Peter Grünberg Institute, Jülich Research Centre, 52425 Jülich, Germany.
§Current address: Institute of Physics, Karlsruhe Institute of Technology (KIT), 76131 Karlsruhe, Germany.
¶Current address: Faculty of Mathematics and Natural Sciences-Physics Department, Bergische Universität Wuppertal, 42119 Wuppertal, Germany.

Introduction

The versatility of carbon cages as robust hosts for various atoms, ions, and more complex endohedral species led to their frequent use in the design of endohedral fullerenes with unusual electronic and magnetic properties.[1–10] The fullerene cage itself can be further modified by a substitution of carbon with heteroatoms. When a heteroatom is nitrogen, the substitution products are known as azafullerenes.[11,12] As a nitrogen atom has one more electron than carbon, azafullerenes have a different electronic structure when compared to all-carbon fullerenes. For instance, the azafullerene $C_{59}N$ dimerizes spontaneously with the formation of a single interfullerene bond.[12,13] Azafullerenes with endohedral metal atoms were discovered in 2008, when Dorn *et al.* isolated and structurally characterized two $M_2@C_{79}N$ compounds with M = Y and Tb.[14] Whereas the C_{80}-I_h cage in normal endohedral metallofullerenes is stabilized by a metal-to-fullerene transfer of 6 electrons,[15] replacement of one carbon by nitrogen effectively contributes one extra electron to the fullerene π-system. The endohedral unit therefore only has to transfer five electrons to the fullerene cage to stabilize its electronic structure. Thus, the formal charge distribution in dimetallo-azafullerenes is $(M_2)^{5+}@(C_{79}N)^{5-}$. A single valence electron in the endohedral M_2^{5+} dimer populates the M–M bonding orbital (Fig. 1a).

Dimetallo-azafullerenes form a subclass of rare-earth based dimetallofullerenes featuring a single-electron metal–metal bond.[16] These molecules gained particular interest during recent years because of their interesting magnetic properties.[17–29] Delocalization of a valence electron between two lanthanide ions results in giant magnetic coupling in the endohedral metal dimer with a formal $[M^{3+}–e–M^{3+}]$ configuration. For metal ions exhibiting axial single-ion magnetic anisotropy in these settings, like Dy and Tb, strong coupling results in robust single-molecule magnetism with enhanced blocking temperature of magnetization and very broad magnetic hysteresis.[23–25,30] In particular, *ab initio* calculations indicated that single-ion quantization axes of Tb^{3+} ions in $Tb_2@C_{79}N$ are almost parallel to the Tb–Tb axis (Fig. 1b).[30] The almost collinear arrangement of Tb magnetic moments and the strong ferromagnetic coupling *via* unpaired electron result in high stability of the giant-spin state and its reluctance to magnetization reversal. As a result, magnetic hysteresis in powder samples of $Tb_2@C_{79}N$ was observed up to 27 K, with 100-second blocking temperature of magnetization near 24 K.[30] In fact, Tb-based dimetallofullerenes, $Tb_2@C_{79}N$ (ref. 30) and $Tb_2@C_{80}(CH_2Ph)$ (ref. 23), are among the strongest single-molecule magnets (SMMs) second to only some metallocenium-based SMMs,[31–34] and show the highest hysteresis temperatures among air-stable SMMs.

An important advantage of metallofullerenes as molecular magnets is the high thermal and chemical stability of fullerene cages. It not only makes dimetallofullerenes air-stable, despite the unconventional oxidation state of endohedral lanthanides, but also allows deposition of metallofullerenes on conducting substrates by sublimation or solution-based self-assembly. Sustained magnetic bistability in a thin film, a monolayer, and eventually a single molecule in contact with a conducting substrate is an important prerequisite for the use of SMMs in nanoscale spintronics. However, a realization of hysteretic behaviour in monolayers is not straightforward and was demonstrated only for a handful of SMMs,[35–55] including some metallofullerene-SMMs.[56–62] The nitride clusterfullerenes $Dy_2ScN@C_{80}$ and $DySc_2N@C_{80}$ were shown to maintain their SMM properties in monolayers on metallic substrates.[56–60] Even more promising are recent studies of $Dy_2@C_{80}(CH_2Ph)$ deposited onto graphene[61] and $Tb_2@C_{80}(CH_2Ph)$ on graphene and HOPG,[62] which demonstrated that dimetallofullerenes with single-electron lanthanide–lanthanide bonds can also sustain their superb SMM performance in monolayers. Magnetic hysteresis in these monolayers was observed at considerably higher temperatures than in all other surface-supported SMMs, reaching 28 K for a self-assembled monolayer of $Tb_2@C_{80}(CH_2Ph)$ derivative.[62] Unlike

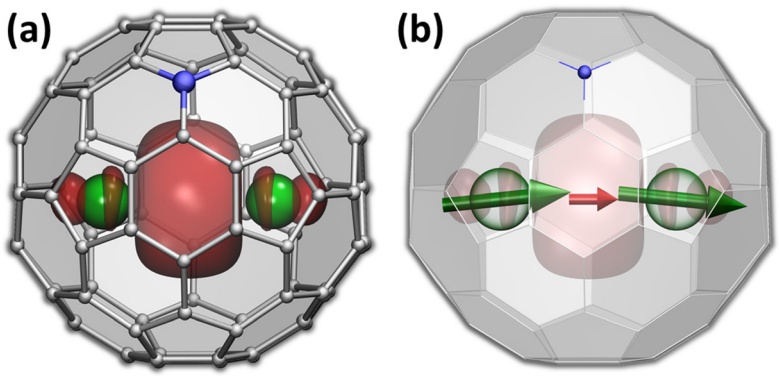

Fig. 1 (a) Molecular structure of $Tb_2@C_{79}N$ with valence spin density isosurface corresponding to the singly-occupied Tb–Tb bonding orbital; Tb is green, N is blue, carbons are grey. (b) Alignment of magnetic moments in $Tb_2@C_{79}N$; green arrows – localized Tb-4f moments, red arrow – unpaired electron spin residing on the Tb–Tb bonding molecular orbital.

$M_2@C_{80}(CH_2Ph)$ derivatives, $Tb_2@C_{79}N$ is free from exohedral organic group, which makes it sufficiently thermally stable for the growth of thin films by sublimation in ultrahigh-vacuum conditions. In this work, we report on the deposition of submonolayers of $Tb_2@C_{79}N$ onto Au(111) and Cu(111) substrates and the electronic and magnetic properties thereof studied by scanning-tunneling microscopy, DFT calculations, and synchrotron-based X-ray absorption spectroscopy (XAS). The influence of the fullerene–substrate interaction on the electronic and magnetic states is further evaluated by introducing thin layers of insulators, MgO and h-BN, between fullerenes and metallic substrates.

Methods

$Tb_2@C_{79}N$ was obtained by arc-discharge evaporation of hollow graphite rods filled with Tb_4O_7 in nitrogen-containing atmosphere and separated from other Tb-EMFs by HPLC following ref. 14 with modifications introduced in ref. 30.

The surfaces of Au(111) and Cu(111) single crystals were prepared by repeated Ar^+-sputtering and annealing cycles. An h-BN monolayer on Rh(111) was prepared according to ref. 63 and 64, and before evaporation of fullerenes, the wafer was annealed in UHV at 1100 K for 15 min. The thin film of MgO on Ag(100) was grown by sublimation of Mg in O_2 atmosphere (10^{-6} mbar) while keeping the substrate at 645 K; the film thickness determined by XAS at the Mg-K edge was in the range of 5 monolayers.

For the surface deposition, $Tb_2@C_{79}N$ was transferred by drop-casting to a crucible of a custom-made molecular evaporator, whose design allowed reducing the distance to the substrate to 4–5 cm. The samples were degassed for several hours at 400 K under high vacuum to remove the traces of solvent. Evaporation then proceeded at 700–710 K, giving submonolayer coverage after 5 min. During evaporation of fullerenes, all substrates were kept at room temperature.

Low-temperature STM measurements were performed at the PEARL beamline[65] (Swiss Light Source, Paul Scherrer Institute) using an Omicron LT-STM microscope with the samples cooled to 4.8 K. Topography and dI/dU maps were measured in constant-current mode, while dI/dU curves were obtained in constant height mode. Spectroscopy data were measured through lock-in detection of the ac tunnel current driven by an 877 Hz, 5 mV rms signal added to the junction bias, produced by a STANFORD SR830 amplifier.

X-ray photoelectron spectroscopy (XPS) measurements were also performed at PEARL for submonolayer and multilayer (*ca.* 0.3 ML and 3 ML coverage) of $Tb_2@C_{79}N$ deposited onto Cu (111), the samples for XPS measurements were cooled to 77 K.

Magnetic properties of $Tb_2@C_{79}N$ layers on various substrates were studied by X-ray magnetic circular dichroism (XMCD) with synchrotron radiation at the X-Treme beamline[66] (Swiss Light Source, Paul Scherrer Institute). Deposition conditions on Au(111) and Cu(111) substrates were the same as for the experiments at the PEARL beamline, and the formation of submonolayers was confirmed *in situ* by room-temperature STM measurements shown in ESI.† In XMCD measurements, the magnetic field was collinear with the X-ray beam, and X-ray absorption was measured in the total electron yield mode. The photon flux on the sample was in the range of $0.3–4 \times 10^{-2}$ photons nm^{-2} s^{-1}. Each measured spectrum was normalized to the intensity of the pre-edge signal, and then the broad background was subtracted. Thus, the XAS signal intensity reported in the paper corresponds to the normalized increase of the XAS due to the specific absorption at the Tb-$M_{4,5}$ edge over the background signal. Non-polarized XAS intensity is defined as XAS = ($I^+ + I^-$), XMCD intensity is ($I^- - I^+$). When XMCD intensities are plotted in %, the XMCD signal is divided by the XAS intensity at its maximum. In the measurement of magnetization curves, I^+ or I^- intensity during each magnetic field sweep was measured at fixed energies corresponding to the maximum of XMCD signal and to the pre-edge energy. In the magnetic hysteresis and angular dependence plots, the ($I^- - I^+$) values are divided by the ($I^+ + I^-$) sum, giving normalized XMCD, denoted as XMCD/XAS. Sum rule analysis for estimation of Tb-4f magnetic moments was performed only for $Tb_2@C_{79}N$ on Au(111) and MgO|Ag (100) substrates, because the strong non-linear background of Cu(111) prevents an accurate estimation of integral values, whereas on h-BN|Rh(111) the signal-to-noise ratio was too low.

DFT modeling of the $Tb_2@C_{79}N$ molecule placed on Au (111), Cu(111), and MgO(100) substrates were performed at the PBE-D level with PAW potentials using the VASP 5.0 code.[67–71] The 4f-in-core potentials used for Tb allowed DFT calculation without explicit treatment of 4f electrons. Metallic Cu(111) and Au(111) substrates were modelled as slabs of 6 atomic layers with lateral unit cells of 12.76 Å (Cu) and 14.43 Å (Au). MgO (100) was described by 4 atomic layers with the lateral unit cell of 12.65 Å. At these intermolecular distances, fullerene–fullerene interactions are presumed to be rather weak. In the course of optimization, both the fullerene and the substrate atomic positions were refined; uncertainty of the relative energies with the numerical settings used in the calculations did not exceed 2 meV. Atomic charges were derived from DFT-computed electronic densities using Bader code.[72] Simulations of magnetization curves were performed with PHI code.[73]

Surface deposition and STM characterization of $Tb_2@C_{79}N$ on Au(111) and Cu(111)

Topographies of $Tb_2@C_{79}N$ layers deposited onto Au(111) and Cu(111) are shown in Fig. 2 (see also Fig. S1–S9 in ESI† for additional data). As common for fullerenes on metallic surfaces,[74] $Tb_2@C_{79}N$ molecules on Cu(111) exhibit sufficiently high mobility on the surface of the room temperature substrate to diffuse over the atomically flat terraces. Step edges of the metal substrate act as preferential starting points for the fullerene island growth, eventually leading to stripes of fullerene islands anchored to the step-edges, although some islands were also found on the substrate terraces. Due to the hcp arrangement of the molecules, a pronounced tendency to hexa-

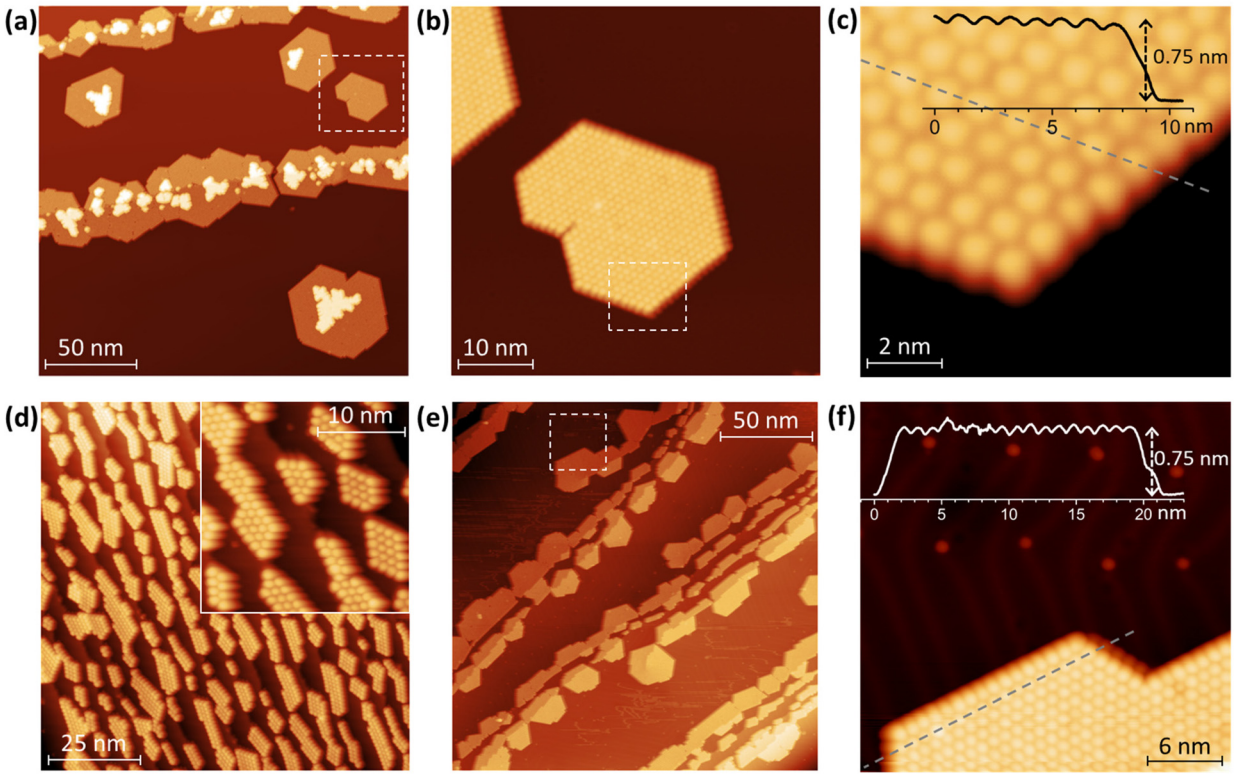

Fig. 2 Topographic images of $Tb_2@C_{79}N$ submonolayer islands on: (a–c) Cu(111), and (d–f) Au(111). (a) Overview of the submonolayer on Cu(111); (b) zoom into the fragment marked by dashed square; (c) further magnification and height profile along the dashed line. (d) Narrow fullerene islands on the Au(111) crystal fragment with many step edges. (e) On Au(111) crystal with larger terraces; (f) magnification of one region on the terrace and the height profile along the dashed line. The characteristic herringbone reconstruction pattern on Au(111) surface can be also seen in (f) along with defects (presumably missing atoms) on the vertices of the herringbone pattern. All measurements are performed at 4.8 K. Measurement parameters on Cu(111): U = +0.8 V, I = 20 pA (a and b) and I = 100 pA (c); on Au(111): U = +0.6 V, I = 20 pA (d), U = −0.5 V, I = 10 pA (d, inset), U = 1 V, I = 20 pA (e and f).

gonally shaped islands is clearly seen (Fig. 2). An onset of the second layer growth is seen on many of the monolayer islands, even though there is still a large area of bare metallic substrate. This is rather uncommon for fullerenes, which usually preferentially cover the whole metallic surface.

On the fragment of the Au(111) crystal with many edge-steps, $Tb_2@C_{79}N$ molecules arrange into arrays of narrow aligned stripes (Fig. 2d and Fig. S8†). This indicates that deposition onto vicinal surfaces may be used in future to create aligned fullerene ribbons with controlled width.[75] On the larger Au(111) terraces, the morphology of the $Tb_2@C_{79}N$ submonolayer is similar to that on Cu(111) except for a much smaller degree of the second layer formation (Fig. 2e and f). Lateral and vertical parameters of the islands on Au(111) are similar to those on Cu(111). The apparent height of fullerene molecules determined from height profiles measured at the bias voltage of +0.8 V is 7.5(1) Å, whereas the lateral size of the hexagonal monolayer lattice is 10.7(3) Å.

Further details of the electronic structure near the Fermi level were studied by scanning tunneling spectroscopy (STS); for technical reasons, the measurements were limited to the ±1 V window. The spectra measured on several $Tb_2@C_{79}N$ islands on Cu(111) can be divided into three groups with slightly different position of the HOMO peak varying between −0.58 V and −0.64 V (Fig. 3a and Fig. S5†). In the LUMO range, no well-defined peaks can be seen. Instead, dI/dU grows continuously with the increase of the bias voltage above +0.5 V. The transport gap in the $Tb_2@C_{79}N$ monolayer on Cu(111) varies in the range of 1.05–1.12 V. The measurements did not reveal pronounced features near the Fermi level.

Measurements over a double-layer of $Tb_2@C_{79}N$ demonstrate a completely different STS profile with the peak at +0.5 V, presumably derived from the LUMO and accompanied by a negative differential conductance feature at the more positive bias (Fig. 3a and Fig. S6†). The transport gap for the double layer is increased beyond 1.5 V, and the HOMO-derived peak cannot be observed in the available voltage window. Both the negative differential conductance and the increase of the gap are consistent with the double-layer structure. Similar phenomena were observed in STM studies of fullerene C_{60} decoupled from metallic substrates, either in C_{60} double layers or in C_{60} deposited on top of other organic molecules.[76–79]

A $Tb_2@C_{79}N$ monolayer on Au(111) has a similar STS pattern to that on Cu(111) with a well-defined HOMO peak, a flat region around the Fermi level, and a steady increase of dI/dU above +0.6 V (Fig. 3b and Fig. S9†). For one of the islands,

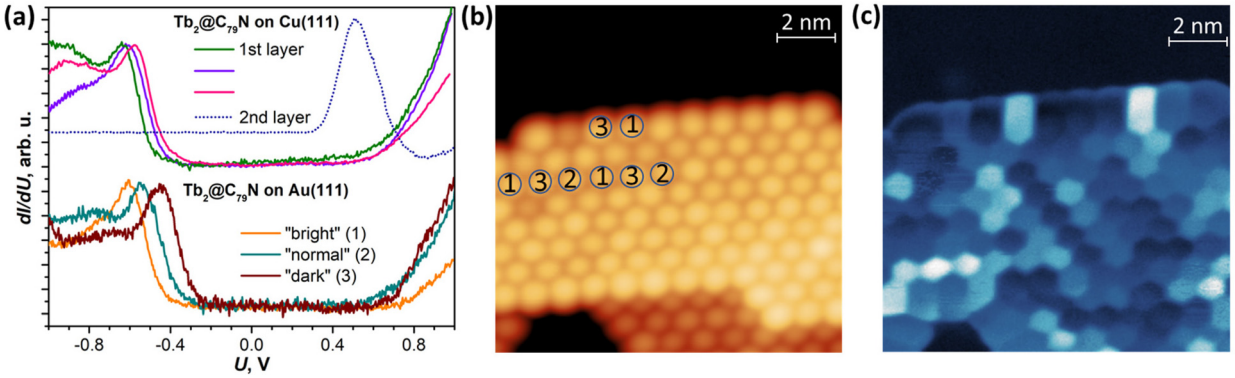

Fig. 3 (a) Top: dI/dU curves measured over $Tb_2@C_{79}N$ islands on Cu(111) over the first layer (three different types) and over the 2nd layer; bottom: dI/dU curves measured over $Tb_2@C_{79}N$ monolayer island on Au(111), shown in (b). The curves are averaged over three different molecular types described in (b) and (c), and for the sake of comparison are normalized to the current of the HOMO peak. (b) Topography of the $Tb_2@C_{79}N$ monolayer island on Au(111) (the molecules on which dI/dU curves were measured are marked by encircled 1, 2, and 3, U = −0.632 V, I = 20 pA); (c) dI/dU map of the same fragment at U = −0.632 V, I = 20 pA, dU = 0.5 mV rms.

we performed dI/dU mapping at U = −0.632 V, near the HOMO-derived peak. Whereas topography of the island shows similar height for all fullerene molecules (Fig. 3b), the dI/dU map reveals strong inhomogeneity with considerable variation of the brightness between different molecules (Fig. 3c). STS measurements at different molecules showed the variation of the HOMO peak from −0.45 to −0.61 eV as well as the variation of the transport gap from 0.95 to 1.18 V (Fig. 3a and Fig. S9†). We tentatively assign this variability to the different orientations of $Tb_2@C_{79}N$ molecules in monolayers as well as different coordination geometry of the cage and metal substrate (the cells of the fullerene monolayer and metallic substrates are not commensurate). Similar variability of the MO peak caused by different molecular orientations was found in a C_{60} monolayer on Cu(100).[80] Interestingly, the variation of the energies and the gap is more pronounced on Au(111) than on Cu(111), showing that $Tb_2@C_{79}N$ molecules are more ordered on copper. This agrees with the results of XMCD studies discussed below, which show a considerably higher degree of ordering of Tb_2 dimers in monolayers on Cu(111).

XPS and valence-band PES

DFT calculations discussed below showed that among the studied substrates, Cu(111) exhibits the strongest interactions with $Tb_2@C_{79}N$ molecules. Thus, $Tb_2@C_{79}N$ deposited on Cu(111) was studied by XPS using excitation at 800 eV. In addition to a submonolayer with a coverage of approximately 0.3 ML as estimated by STM, the measurements were also performed for a multilayer sample with a thickness of about 3 ML.

The N 1s signal of $Tb_2@C_{79}N$ is found at the binding energy of 401 eV. Neither the peak energy nor its shape changes with the level of coverage (Fig. 4a). This indicates that the nitrogen site of the azafullerene is not involved in the strong interaction with the copper substrate. Presumably, the molecules are landing on Cu(111) with the nitrogen oriented upside to avoid its contact with the metallic substrate (see results of DFT calculation below). The N 1s binding energy in $Tb_2@C_{79}N$ is close to the N 1s binding energy in nitrogen-substituted C-sp^2 compounds. For instance, pyridinic (6-membered ring) and pyrrolic (5-membered ring) nitrogen gives XPS signals at 398.3 ± 0.3 eV and 400.1 ± 0.3 eV,[81] respectively, *N*-substituted graphene/graphite has a peak at 400–402 eV, whereas the N 1s binding energy in azafullerene $C_{59}N$ is 400.7 eV.[81,82] For comparison, the N 1s binding energy of the endohedral nitride ion (N^{3-}) in metallofullerenes of the $M_3N@C_{2n}$ family is noticeably lower, 396–397 eV: 396.1 eV in $Sc_3N@C_{78}$,[83] 396.9 eV in $Sc_3N@C_{80}$,[84] and 396.8 eV in $TbSc_2N@C_{80}$.[85]

The C 1s photoemission peak of $Tb_2@C_{79}N$ multilayer has a maximum at 284.6 eV and full width at half-maximum of 1.1 eV. The peak energy is somewhat lower than in C_{60} (285.0–285.2 eV)[86,87] or in metallofullerenes $M_3N@C_{80}$ with C_{80}-I_h cage (285.2 eV for M = Sc,[84] 285.4 eV for M = Tm,[88] 285.9 eV for M = Dy[89]). The linewidth as well as the asymmetric shape of the peak is in line with those of EMFs with C_{80} fullerene cage.[84,85,88,89] The C 1s peak of $Tb_2@C_{79}N$ shows noticeable variation of the band shape and increase of the binding energy by *ca.* 0.2 eV when going from 3 ML to 0.3 ML coverage. Presumably, the fullerene–substrate interactions have a non-negligible influence on the C 1s core levels, unlike the N 1s level of the cage nitrogen. But the shift is not sufficiently strong to make a definitive conclusion on its nature. For comparison, in C_{60} adsorbed on Ag(110), a system with a strong fullerene–metal interactions and a sizeable charge transfer, the C 1s peak shifts to a lower binding energy by 0.7 eV on going from a monolayer to a multilayer coverage.[90]

We also studied valence-band photoelectron spectra (PES) using X-ray excitation with photon energy $h\nu_{ex}$ varied in the 1228–1242 eV range. At $h\nu_{ex}$ = 1228 eV, the PES spectrum is dominated by occupied states of Cu with strong peaks at the binding energies of 1.5–5.5 eV. Carbon and terbium have very small cross sections at this excitation energy. But when $h\nu_{ex}$ is scanned through the Tb-M_5 (3d → 4f) absorption edge, the resonantly enhanced Tb-4f photoemission appears at 5–15 eV

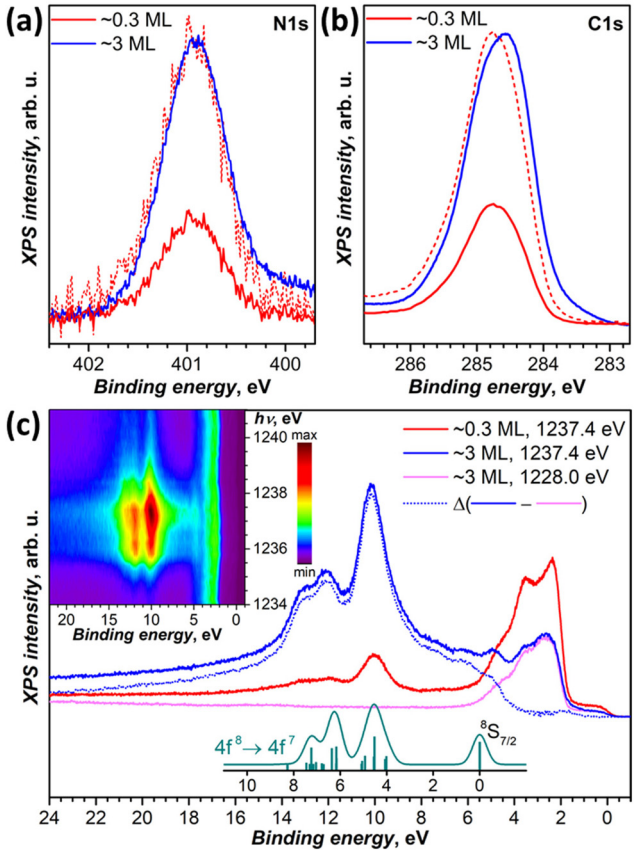

Fig. 4 (a and b) XPS spectra of $Tb_2@C_{79}N$ on Cu(111) in the N 1s (a) and C 1s (b) energy range, measurements are performed at 77 K with excitation at 800 eV for submonolayer (~0.3 ML, red curves) and multilayer (~3 ML, blue curves); dashed red curves are spectra of the submonolayer sample scaled to match intensity of the multilayer. (c) Valence band photoelectron spectra with excitation at 1228 eV (off-resonance, magenta) and at 1237.4 eV (in resonance with 3d → 4f excitation of Tb at the M_5 edge) compared to theoretical intensity of $4f^8 \rightarrow 4f^7$ ionization transitions as calculated by Gerken[91] (cyan, vertical bars are individual transition, and the curve is Gaussian broadening with the peak width of 0.6 eV). Blue dotted curve is the difference between in-resonance and off-resonance spectra. The inset shows variation of the PES intensity with the excitation photon energy between 1234 and 1241 eV measured with the step of 0.2 eV.

below the Fermi level. The strongest Tb-4f emission is observed at $h\nu_{ex}$ = 1237.4 eV (Fig. 4c). The Cu-based photoemission intensity remains virtually constant at these excitation energies. The spectra of 0.3 ML and 3 ML samples have the same resonant Tb-4f photoemission profile, which points to the absence of a strong interaction between Tb-4f electrons and the substrate. This is not surprising in the view of the localized nature of 4f electrons and shielding of endohedral Tb ions by the fullerene cage. The electron escape depth is short and most of the signal comes from the outermost layers. As a result, when the coverage of the substrate is increased from 0.3 to 3 ML, the resonant PES signal of Tb-4f increased considerably, whereas that of copper substrate decreased almost twice.

Off-resonance $4f^8 \rightarrow 4f^7$ photoemission intensity was computed by Gerken using the intermediate interaction model.[91] According to his results, ionization of Tb^{3+} should give a stand-alone peak at the $4f^7$ ground state ($^8S_{7/2}$) and a complex multiplet at higher energies, between 4 and 8 eV above the $^8S_{7/2}$-derived transition. The predicted multiplet structure corresponds well to a peak at 10.1 eV and a double peak at 12.1/12.9 eV below the Fermi level in the resonant PES spectrum of $Tb_2@C_{79}N$. At the same time, the $^8S_{7/2}$ transition does not appear as sharp and well-resolved as predicted by theory. Instead, subtraction of the off-resonance spectrum leaves a broad band with multiple unresolved features at the binding energies of 5–7 eV. Presumably, the difference may be caused by the resonance nature of the spectra. Note that earlier the same theory gave very good agreement with X-ray valence band PES spectra of metallofullerenes $Dy_3N@C_{80}$,[89] $Tm_3N@C_{80}$,[92] and $Tm@C_{82}$[93] excited with Al Kα radiation (1486.6 eV). At that energy, the cross section of lanthanides is also very high, but there is no resonance with Dy-M_5 or Tm-M_5 absorption edges.

Computational modeling

DFT calculations were performed to understand how interactions with metallic substrates can affect the molecular ordering and electronic structure of $Tb_2@C_{79}N$. In particular, we aimed to understand how the presence of the nitrogen atom in the fullerene cage affects the adsorption geometry of the molecule. Another question of interest was how Tb_2 dimers are preferentially oriented inside the fullerene cage when it interacts with a substrate. Computations of an isolated $Tb_2@C_{79}N$ molecule revealed that the nitrogen atom is located at the [5,6,6] position and that metal atoms tend to avoid close contact with nitrogen.[14,30] The lowest energies were found then for the conformers, in which Tb_2 atoms are located on the plane oriented perpendicular to the axis passing through the center of mass (CM) and the nitrogen atom. At the same time, rotation of the metal dimer in this plane leads to small energy variations, indicating that there is a certain flexibility for the dimer position. Our earlier theoretical studies of surface-supported $Dy_2ScN@C_{80}$ molecules showed that metallic substrates exhibit a significant orientational effect on the endohedral cluster.[57] The latter tends to orient itself parallel to the surface to avoid interactions of endohedral metal atoms with a surface-contacted fragment of the fullerene cage. To summarize, these findings show that a reliable study of metallofullerene on the surface should consider various degrees of freedom of the whole molecule as well as its endohedral unit.

For a comprehensive description of $Tb_2@C_{79}N$ on Cu(111), Au(111), and MgO(100) substrates, we generated 240 starting configurations of an adsorbed $Tb_2@C_{79}N$ molecule with different positions of the nitrogen and endohedral Tb_2 dimer on each substrate[94] and optimized them at the DFT level (see Methods for further details and ESI† for details of structure generation). Even with this large number of structures, complete sampling cannot be guaranteed because the parameter

space is immense, but it is representative enough to find general trends in the preferable configurations. Two angles defined in Fig. 5a are used in the further discussion to parameterize the $Tb_2@C_{79}N$ structure on the surface. The angle between the Tb_2 bond and the normal to the substrate z is denoted as $\phi(Tb_2–z)$; the values of ϕ close to 90° correspond to the parallel orientation of the Tb_2 dimer *versus* the surface. The nitrogen position with respect to the substrate is described by the angle θ(N–CM–z) between the N–CM axis and the normal to the surface z; small values of θ correspond to the nitrogen atom facing the surface, whereas the values close to 180° correspond to the nitrogen facing upwards. Note that for the vast majority of optimized structures, the angle between the Tb_2 bond and N–CM axis is within the 75°–90° range.

Fig. 5b–d and Fig. S12† plot distributions of $\phi(Tb_2–z)$ and θ(N–CM–z) angles in optimized structures, whereas their relative energies are encoded in the color of the dots. The range of the relative energies obtained for optimized conformers depends considerably on the substrate. For an isolated $Tb_2@C_{79}N$ molecule, the conformers span the energy range of 100 meV.[30] For adsorbed molecules, the range of the energies increases to 860 meV (on Cu) and 770 meV (on Au). On the insulating MgO(100), the spread of values is reduced to 320 meV, which is still significantly higher than for the isolated molecule.

There is a clear tendency to avoid landing configurations, in which the nitrogen atom of the azafullerene cage is in close contact with the metal substrate. All structures with θ(N–CM–z) less than 20° are among the least stable configurations on

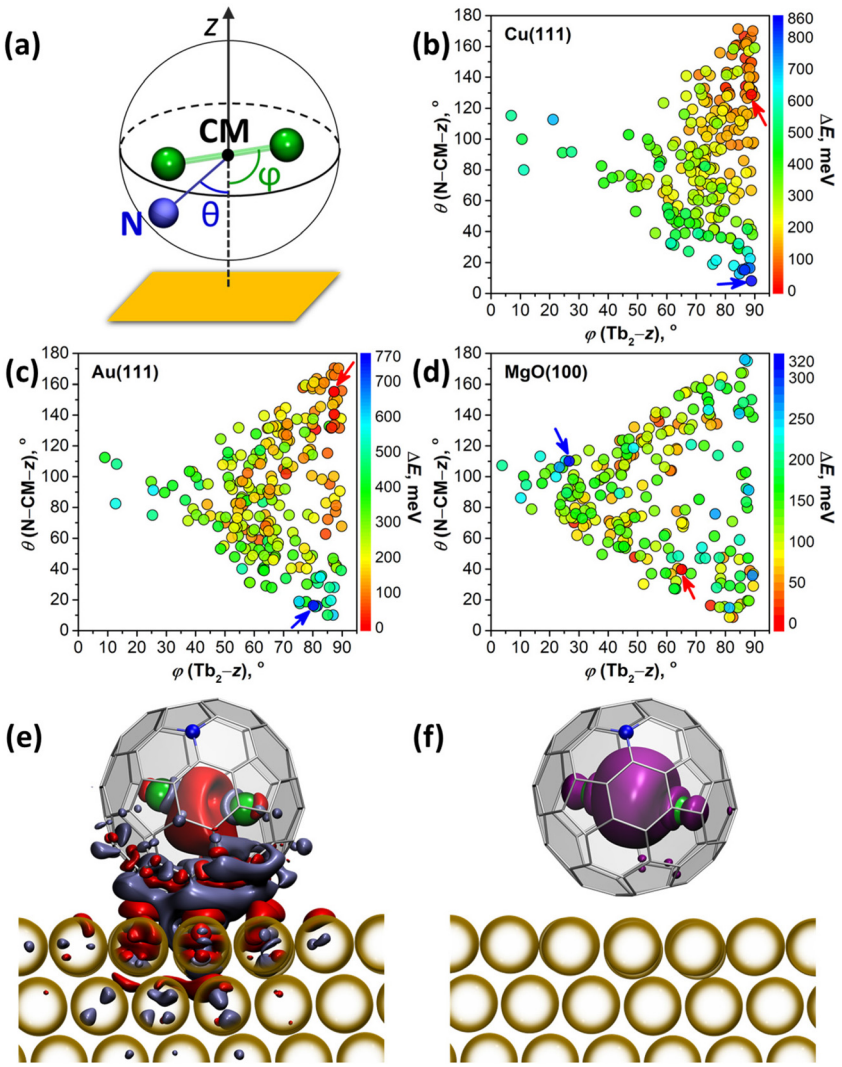

Fig. 5 (a) Definition of the $\phi(Tb_2–z)$ and θ(N–CM–z) angles for an adsorbed $Tb_2@C_{79}N$ molecule, CM is the center of mass, z is the normal to the surface, Tb atoms are shown as green spheres; (b–d) distribution of ϕ and θ angles in DFT optimized structures of $Tb_2@C_{79}N$ molecules adsorbed on Cu(111) (b), Au(111) (c), and MgO(100) (d) with their color-coded relative energies. Red and blue arrows point to the most and least stable structures, respectively. (e) Difference of the electron density for the $Tb_2@C_{79}N$ molecule adsorbed on Au(111) (blue and red isosurfaces mark areas with decrease and increase of the electron density, respectively). (f) Spin density distribution for the structure plotted in (e).

Cu(111) and Au(111). On the other hand, for the most stable structures with ΔE < 100 meV, θ(N–CM–z) angles are higher than 96° on Cu(111) and 59° on Au(111). The avoidance of N-metal contacts is in line with N 1s XPS results for $Tb_2@C_{79}N$ on Cu(111) discussed above. Note that there is no clear preference for the position of nitrogen for $Tb_2@C_{79}N$ molecules on MgO.

Calculations also reveal the preference of the parallel orientation of Tb_2 with respect to metallic substrates. For the most stable structures with ΔE < 100 meV, ϕ(Tb_2–z) angles span the ranges of 73°–90° on Cu(111) and 50°–90° on Au(111). For the cut-off of 200 meV, the ranges increase to 54°–90° on Cu(111) and 39°–90° on Au(111). Thus, the effect is most pronounced for Cu(111), whereas on Au(111) the ordering effect of the substrate is weaker. For MgO, we do not find a preferential orientation of the Tb_2 dimer. The lack of ordering effect on MgO can be explained by the weak electronic interactions between the fullerene π-system and the substrate. This is different on metal substrates, where hybridization of the fullerene π-system with the metal bands is much stronger.

The degree of charge transfer between the $Tb_2@C_{79}N$ molecule and a substrate was determined by Bader analysis (Fig. S14†).[95] Calculations show that $Tb_2@C_{79}N$ molecules attain 0.4–0.6 electrons from Cu(111). On Au(111) the direction of the charge transfer is reversed, and fullerene molecules lose 0.05–0.2 electrons to the substrate. On MgO(100), $Tb_2@C_{79}N$ molecules gain 0.10–0.15 electrons from the surface. Similar sign and magnitude of charging was found earlier for $Dy_2ScN@C_{80}$ on Au(111) and MgO(100) substrates.[57] For Cu(111), the degree of the charge transfer appears to be overestimated by theory, as it leads to a considerable change of the electron density of states and appearance of the features near the Fermi level (Fig. S13†), which could not be observed in the STS measurements (Fig. 3a). Visualization of the difference electron density for $Tb_2@C_{79}N$ on Au(111) in Fig. 5e (see Fig. S15† for Cu(111)) shows that the charge redistribution is mainly localized in the region between the fullerene and the substrate. Some excess of the electron density can be also seen in the area between Tb atoms, but the spin density distribution for this structure (Fig. 5f) proves that the single-electron nature of the Tb–Tb bond is preserved on Au(111).

X-ray absorption studies of $Tb_2@C_{79}N$ films

Submonolayers of $Tb_2@C_{79}N$ on Cu(111) and Au(111) (~0.2 ML, see Fig. S10 and S11† for STM topographies) were studied by X-ray absorption spectroscopy (XAS) at the Tb-$M_{4,5}$ edge with circular-polarized X-rays. Both layers show XAS spectra typical for Tb^{III} (see Fig. 6 for M_5 edge and ESI† for full spectra) and develop X-ray magnetic circular dichroism (XMCD) in the presence of a magnetic field. The maximum of the XMCD signal at 1235 eV was then used to monitor the changes of the monolayer magnetization during magnetic field sweeps described below. As the X-ray beam and magnetic field were aligned parallel in the measurements, the XMCD intensity is proportional to the magnetization in the direction of the beam. Thus, the measurements at different incidences allow the determination of the preferential orientation of magnetic moments in the monolayer. For a $Tb_2@C_{79}N$ monolayer on Au(111), polarized spectra and normalized XMCD intensity for the measurements in normal (90°) and grazing (30°) incidence are very similar (Fig. 6a). Thus, there is no discernable ordering of Tb_2 dimers in $Tb_2@C_{79}N$ adsorbed on gold. A completely different situation is found on Cu(111). Here, the XMCD signal at grazing incidence is 4 times stronger than at normal incidence. Since magnetic moments of Tb ions in $Tb_2@C_{79}N$ are aligned along the Tb–Tb bond (Fig. 1), we conclude that Tb_2 dimers in $Tb_2@C_{79}N$ monolayer on Cu(111) are oriented parallel to the surface.

Magnetic behavior of $Tb_2@C_{79}N$ films on Au(111) and Cu(111)

Before studying the magnetization dynamics in monolayer samples by XMCD, we made reference measurements of the magnetic hysteresis of the $Tb_2@C_{79}N$ multilayer drop-casted onto a gold substrate. The studies of similarly prepared samples by SQUID magnetometry showed broad magnetic hysteresis at T = 2.5 K (Fig. 7a).[30] The magnetic hysteresis recorded by XMCD technique is much narrower, despite the faster sweep rate. The further narrowing was observed when the X-ray flux was increased by a factor of 6 (see also Fig. S16 in ESI†). This proves that the X-ray irradiation considerably accelerates magnetic relaxation in $Tb_2@C_{79}N$. Such X-ray induced demagnetization was reported earlier in monolayers of metallofullerenes[61,62,96] and $TbPc_2$,[46] but the effect in $Tb_2@C_{79}N$ is more pronounced. Further measurements of (sub)monolayer films demonstrate that not only the demagnetization rate but also the population of valence orbitals may be affected by X-ray irradiation through secondary processes.

In contrast to the multilayer sample, submonolayers of $Tb_2@C_{79}N$ on Au(111) and Cu(111) did not show magnetic hysteresis. Instead, they revealed an unexpected shape of the magnetization curves characteristic for a ground state with a small magnetic moment. The effect is especially well seen for Au (111). Magnetization of the sample remains small up to the field of 2.5–4 T, and then increases fast above a certain threshold field. Such a behavior is expected for a system with a moderately-strong antiferromagnetic (afm) coupling of magnetic moments undergoing a metamagnetic transition in high field. While non-magnetized in small external fields, the system develops magnetization in high fields, when the ferromagnetically-coupled state (fm) becomes lower in energy due to the Zeeman effect. Interestingly, the threshold field changes from 2.5 T at the grazing incidence to 4 T at the normal incidence. Thus, there is some anisotropy of the Tb_2 orientation in $Tb_2@C_{79}N$ molecules adsorbed on Au(111), although much less pronounced than on Cu(111), and the parallel alignment is somewhat more preferable here as well. Hence a smaller magnetic field is required to switch between afm and fm states in grazing incidence. Sum rule analysis was performed to estimate the 4f-contribution to the magnetic moment of Tb ions in $Tb_2@C_{79}N$ on Au(111). At 2 K and the field of 6.8 T, the Tb-4f moment ($\mu_{Tb\text{-}4f}$) is estimated as 3 ± 0.5μ_B. This value is considerably smaller than the 4.5μ_B expected for Tb^{3+} ions with

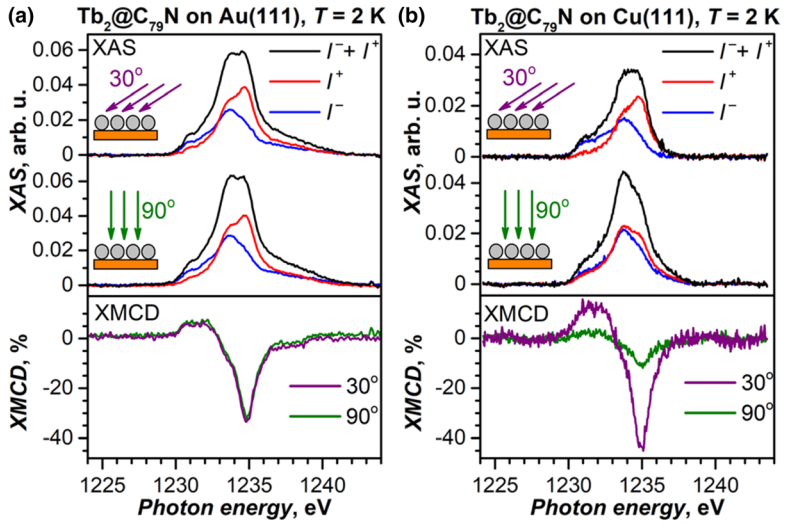

Fig. 6 Tb-M_5 XAS (top panels) and XMCD (bottom panels) spectra of $Tb_2@C_{79}N$ submonolayers (~0.2 ML coverage) on Au(111) (a) and Cu(111) (b). $T \approx 2$ K, $\mu_0 H = 6.8$ T, grazing (30°) and normal (90°) X-ray and magnetic field incidence with respect to the surface. I^+ and I^- are circular polarized XAS spectra, non-polarized XAS is defined as a sum ($I^+ + I^-$), XMCD is defined as a difference ($I^- - I^+$), normalization to the maximum of XAS gives XMCD in %.

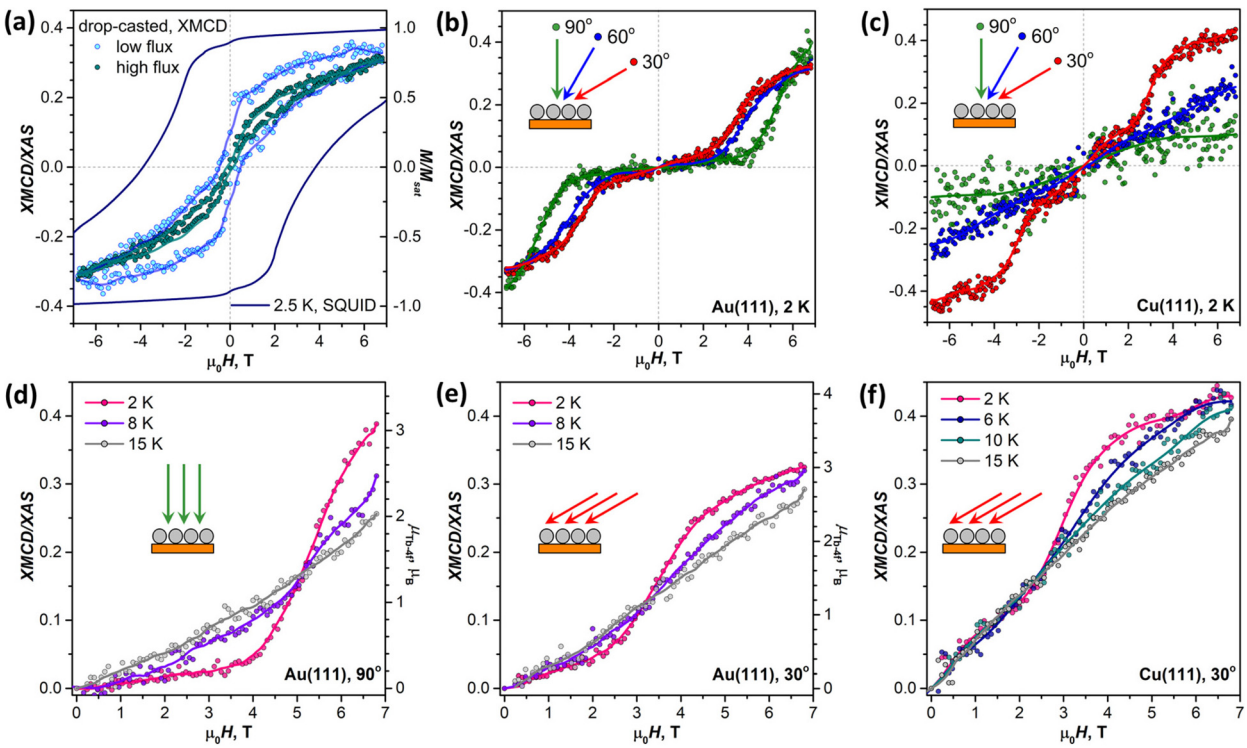

Fig. 7 (a) Magnetic hysteresis of powder $Tb_2@C_{79}N$ measured by SQUID magnetometry (solid line) compared to the hysteresis in $Tb_2@C_{79}N$ multilayer drop-casted onto Au crystal and measured by XMCD with two different X-ray fluxes (sweep rate 0.2 T min^{-1} for SQUID and 2 T min^{-1} for XMCD measurements, $T \approx 2$ K, X-ray flux is varied from 0.3×10^{-2} to 2×10^{-2} photons nm^{-2} s^{-1}, respectively). (b) Magnetization curves of $Tb_2@C_{79}N$ submonolayer on Au(111) measured by XMCD with three different incidence angles, $T \approx 2$ K, the field was ramped from +6.8 T to −6.8 T and back to +6.8 T. (c) Magnetization curves of $Tb_2@C_{79}N$ submonolayer on Cu(111) measured by XMCD with three different incidence angles, $T \approx 2$ K. (d) Averaged magnetization curves of $Tb_2@C_{79}N$ submonolayer on Au(111) measured at different temperatures in normal incidence (90°). (e) Averaged magnetization curves of $Tb_2@C_{79}N$ submonolayer on Au(111) measured at different temperatures in grazing incidence (30°). (f) Averaged magnetization curves of $Tb_2@C_{79}N$ submonolayer on Cu(111) measured at different temperatures in grazing incidence (30°). In all panels, dots are experimental measurements, whereas lines are smoothed experimental data shown to guide the eye; data shown in (d–f) are averaged over four segments ([0 → 6.8 T], [0 → −6.8 T], [6.8 T → 0], and [−6.8 T → 0]). Tb-4f magnetic moment scale ($\mu_{Tb\text{-}4f}$) in (d) and (e) is obtained from a sum rule analysis.

easy-axis magnetic anisotropy in a disordered monolayer, which is not surprising given the fact that the magnetization is not saturated yet in this field (Fig. 7).

Similar switching between afm and fm states is found in submonolayer of $Tb_2@C_{79}N$ on Cu(111). The switching field in grazing incidence is also close to 2.5 T as for Au(111). However, the transition between afm and fm states is not as pronounced as on Au(111). Besides, the sample on Cu(111) shows higher residual magnetization in smaller fields indicating that the molecules with afm and fm ground state can co-exist on Cu(111).

When temperature is increased from 2 K to 15 K (Fig. 7d–f), the transition between afm and fm states becomes less sharp. Presumably, the fm state becomes more thermally accessible at smaller fields, when it is still higher in energy than the afm state. At the same time, magnetization in higher fields, when the fm state is dominant, is smaller because the system requires a higher field to reach the saturation.

$Tb_2@C_{79}N$ films on h-BN|Rh(111) and MgO|Ag(100)

To decrease the electronic coupling of $Tb_2@C_{79}N$ molecules with the substrate, we then used a thin layer of semiconductor (monolayer h-BN on Rh(111)) or insulator (5 ML of MgO on Ag(100)). Fullerene layers on these substrates were prepared by thermal evaporation. For MgO(5 ML)|Ag(100), the evaporation was carried out at a higher temperature and gave 1.5 ML coverage as determined by comparison of Tb-$M_{4,5}$ XAS intensity to that of $TbPc_2$ on MgO|Ag(100) from ref. 46 and 51. Tb-M_5 XAS and XMCD spectra of $Tb_2@C_{79}N$ on both substrates are shown in Fig. 8. The measurements in grazing incidence give a somewhat higher XMCD signal, indicating a slight preference of the parallel orientation of Tb_2 dimer with respect to the surface, but the effect is less pronounced than on Cu(111) in Fig. 6b.

In Fig. 9, magnetization curves measured at 2 K are compared to 30 K measurements. The concave shape of the low-temperature curves again points to the prevalence of the afm state in low fields, although it should co-exist with a fraction of molecules with large magnetic moment. Thus, the electronic decoupling of $Tb_2@C_{79}N$ molecules from metals does not eliminate the afm ground state for some of them. At 30 K, magnetization curves show more typical outward curvature in the whole field range. Gradual transition from inward to outward curvature can be seen at intermediate temperatures (15 K and 25 K in Fig. 9c and d). Sum rule analysis for 30 K and 6.8 T gives the $\mu_{Tb\text{-}4f}$ values of $3 \pm 0.5\mu_B$, similar to the estimation on Au(111). It is clear from the shape of the magnetization curves that the magnetization is not saturated at this field. At lower temperatures, the $\mu_{Tb\text{-}4f}$ values at 6.8 T are even smaller (Fig. 9 and 10).

At 2 K, $Tb_2@C_{79}N$ on h-BN|Rh(111) and MgO|Ag(100) exhibits narrow magnetic hysteresis. Hysteresis on MgO|Ag(100) remains open up to 25 K (Fig. 9d). No hysteresis can be found at 30 K (Fig. 9a and b). The closing temperature of hysteresis in $Tb_2@C_{79}N$ on MgO|Ag(100) agrees with bulk magnetic measurement of $Tb_2@C_{79}N$[30] as well as bulk and monolayer measurements in monolayers of $Tb_2@C_{80}(CH_2Ph)$ derivatives on graphitic substrates.[62]

The origin of the antiferromagnetic state

The afm ground state of $Tb_2@C_{79}N$ monolayers found in XMCD measurements was completely unexpected. Strong ferromagnetic coupling of Tb moments in $Tb_2@C_{79}N$ is caused by the unpaired valence electron delocalized between two Tb ions (Fig. 1). The change of the magnetic ground state may indicate that the Tb–Tb bonding orbital changed its occupation by acquiring an additional electron (Fig. 10a). Earlier,

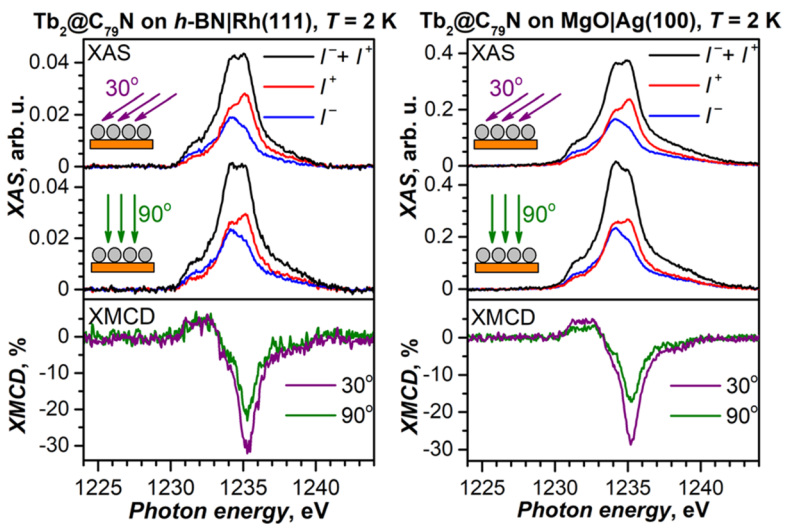

Fig. 8 Tb-M_5 XAS (top panels) and XMCD (bottom panels) spectra of $Tb_2@C_{79}N$ evaporated onto h-BN|Rh(111) (left) and MgO|Ag(100) (right). $T \approx 2$ K, $\mu_0 H = 6.8$ T, grazing (30°) and normal (90°) X-ray and magnetic field incidence with respect to the surface. I^+ and I^- are circular polarized XAS spectra, non-polarized XAS is defined as a sum ($I^+ + I^-$), XMCD is defined as a difference ($I^- - I^+$), normalization to the maximum of XAS gives XMCD in %.

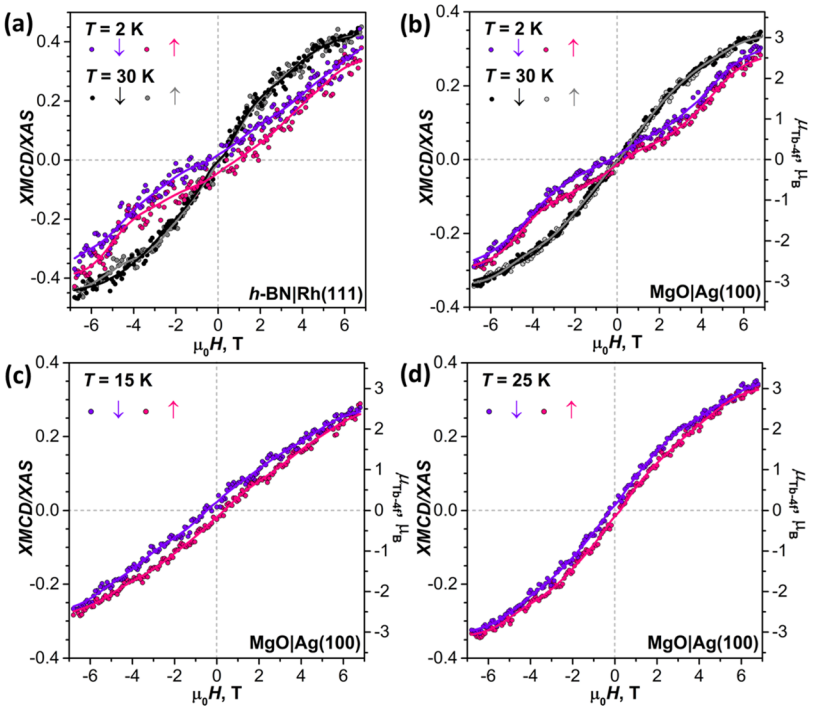

Fig. 9 (a) Magnetization curves of a $Tb_2@C_{79}N$ submonolayer on h-BN|Rh(111) at 2 K and 30 K. (b) Magnetization curves of $Tb_2@C_{79}N$ 1.5 ML on MgO|Ag(100) at 2 K and 30 K. (c and d) Magnetic hysteresis of $Tb_2@C_{79}N$ 1.5 ML on MgO|Ag(100) measured at 15 K (c) and 25 K (d). All curves are measured in grazing incidence (30°); magnetic field sweep rate is 1.5 T min^{-1}; dots are experimental measurements, lines are smoothed experimental data and are shown to guide the eye only; arrows denote the measurements during decrease (↓) and increase (↑) of the magnetic field; Tb-4f magnetic moment scale ($\mu_{Tb\text{-}4f}$) is obtained from a sum rule analysis.

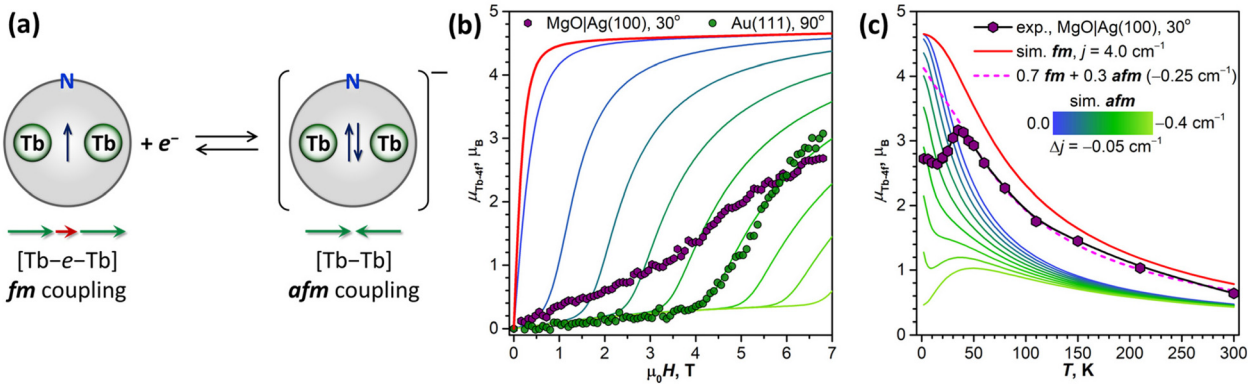

Fig. 10 (a) Schematic description of the electron trapping by the SOMO of $Tb_2@C_{79}N$ leading to $Tb_2@C_{79}N^-$ anion with two-fold occupied Tb–Tb bonding MO and antiferromagnetic coupling of magnetic moments; green arrows denote Tb-4f magnetic moments, red arrow denotes magnetic moment of the unpaired valence electron. (b) Magnetization curves of $Tb_2@C_{79}N$ on MgO|Ag(100) and Au(111) measured at $T \approx 2$ K and compared to the results of simulations for fm and afm coupling of Tb-4f magnetic moments, the coloring scheme is the same as in (c). (c) Temperature dependence of Tb-4f magnetic moment in $Tb_2@C_{79}N$ 1.5 ML on MgO|Ag(100) measured by XMCD at 6.8 T in grazing incidence and compared to the results of simulations for ferromagnetic (fm) and antiferromagnetic (afm) coupling of Tb-4f magnetic moments with different values of the coupling constant j_{12}; dashed line is a simulation for a mixture of molecules with fm (70%) and afm (30%) ground states.

we demonstrated that single-electron reduction of dimetallofullerenes $M_2@C_{80}(CH_2Ph)$ in solution leads to stable anions with two-fold occupied M–M bonding orbital and reduced magnetic anisotropy.[16,23] In the absence of an unpaired valence electron, lanthanide–lanthanide interactions *via* two-electron M–M bond are presumably antiferromagnetic (Fig. 10a). Thus, unusual magnetic behavior is not caused by intact $Tb_2@C_{79}N$ molecules, but results from the trapping of an extra electron.

Reduction of adsorbed fullerenes could be caused by their strong hybridization with the metallic substrate and an electron transfer from the metal to the Tb–Tb bonding SOMO, as

predicted by DFT for $Tb_2@C_{79}N$ on Cu(111). In case of a fractional charge transfer between fullerene and metal, one may expect a non-zero DOS at the Fermi level, which however is not validated by the STM/STS results for $Tb_2@C_{79}N$ on Cu(111) and Au(111), showing a considerable HOMO–LUMO gap (Fig. 3a). However, the metal–metal bonding MO hidden inside a fullerene cage may be not well accessible for STM, although we did observe the features of such orbitals in $M_2@C_{80}(CH_2Ph)$ molecules deposited on a graphene|Ir(111) substrate.[97] Besides, when the charge transfer is integer, STS of the adsorbed anion may show a gapped pattern.

Deposition of $Tb_2@C_{79}N$ on thin dielectric layers was aimed at the electronic decoupling of fullerenes from the underlying metals. The persistence of the afm state on h-BN|Rh(111) and MgO|Ag(100) could serve as an indication that the charge transfer from the substrate is not the reason for the unexpected magnetic behavior of $Tb_2@C_{79}N$. However, the charge transfer hypothesis still cannot be fully excluded by these data because there are examples of the electron transfer between Ag and adsorbate on MgO|Ag(100) substrates.[98–104] For instance, pentacene molecules acquire one electron when deposited onto MgO(2 ML)|Ag(100).[99] Variation of the MgO layer thickness and work-function resulted in the co-existence of neutral and charged pentacene molecules, and signatures of the charge transfer were observed up to the MgO thickness of 16 ML.[100] Coexistence of Dy atoms and Dy^+ ions with the ratio depending on the MgO thickness was recently demonstrated for Dy deposited on MgO|Ag(100).[104] Such situations are less documented for adsorbates on h-BN|metal substrates,[105] but not unimaginable either. For instance, C_{60} retains its charge state on h-BN|Ni(111) at low temperature, but the population of its LUMO is increased by 0.4 electrons at room temperature.[106] Thus, there is no fundamental reason why an electron transfer cannot occur across the h-BN or MgO layers, and we cannot fully exclude such a possibility for $Tb_2@C_{79}N$ on h-BN|Rh(111) and MgO|Ag(100). Importantly, a dielectric layer can stabilize the states of adsorbate molecules with an integer charge, whereas the direct contact with metal would usually give hybridized states with fractional charge transfer. Thus, in certain situations a thin dielectric layer may even stabilize the charged state of an adsorbate.

The electron transfer from the substrate is not the only plausible source of the surplus electron. The method employed to study magnetic properties of monolayers, XAS/XMCD, is by no means an innocent technique. The influence of the X-ray flux on the magnetization relaxation and the width of magnetic hysteresis was already discussed above (Fig. 5a). Absorption of an X-ray photon, 3d → 4f excitation, and subsequent decay of the core-hole results in the Auger process forming a cascade of secondary electrons, which are then collected as a drain current from the sample. But some can be trapped in the sample, especially an insulating one, leading to its charging and affecting the energies and intensities of measured signals.[107–109] Although charging effects are not expected to play a strong role for molecular submonolayers on metals, the singly unoccupied Tb–Tb MO buried inside the fullerene cage and thus well-isolated from the substrate may be an efficient trap for such electrons. In this situation, irradiation with an X-rays might generate metastable $Tb_2@C_{79}N^-$ anions and change the magnetic properties of the sample. If our hypothesis on the secondary electron trapping is correct, then the afm state we observe is an artefact of the experimental technique (XMCD) and does not reflect the intrinsic magnetic behavior of the $Tb_2@C_{79}N$ monolayer.

As an alternative to the intramolecular nature of the afm state, one might suggest that the non-magnetic ground state emerges as a result of the intermolecular antiferromagnetic coupling, whereas the charge state and intramolecular ferromagnetic coupling of $Tb_2@C_{79}N$ molecules is preserved. Although we never observed measurable intermolecular magnetic coupling in bulk metallofullerene samples, the situation may be different in a monolayer on a metal, where such interactions may be mediated by conducting electrons of a metallic substrate in the spirit of the Ruderman–Kittel–Kasuya–Yosida mechanism.[110–112] But this would require considerable electronic coupling of the fullerene with the underlying substrate and can be ruled out based on the experiments with h-BN and MgO, unlike the charge-transfer through these layer, which does not require hybridization. Thus, we consider the intramolecular origin of the afm state in $Tb_2@C_{79}N$ monolayers as much more plausible.

Magnetic simulations

To get more insight into the magnetic properties of the $Tb_2@C_{79}N$ monolayer, we simulated magnetization curves for $Tb_2@C_{79}N$ in neutral and anionic states. Description of dimetallofullerenes with single-electron M–M bond used in ref. 19, 23, 24 and 30 is based on a three-center model, including two local Tb-4f moments with spin operators $\hat{J}_{Tb}$ and ligand-field (LF) Hamiltonians $\hat{H}_{LF}$, unpaired electron spin $\hat{s}$, and their exchange interactions, forming the following effective spin Hamiltonian:

$$\hat{H}_{spin} = \hat{H}_{LF'} + \hat{H}_{LF''} - 2j_{12}\hat{J}_{Tb'}\hat{J}_{Tb''} - 2\hat{s}K(\hat{J}_{Tb'} + \hat{J}_{Tb''}) + \hat{H}_{ZEE} \quad (1)$$

where the exchange Hamiltonian includes direct Tb–Tb interaction with the coupling constant j_{12} and exchange interactions between Tb-4f moments and the unpaired electron spin with the exchange constant K, and $\hat{H}_{ZEE}$ is the Zeeman term. Ligand-field parameters were adopted from *ab initio* calculations, predicting moderately-strong uniaxial single-ion anisotropy with $J_z = 6$ ground state.[30] DFT calculations for Gd dimetallofullerenes showed that direct lanthanide–lanthanide coupling is antiferromagnetic but is much smaller than the strong ferromagnetic coupling with the unpaired electron, so that the former could be safely neglected.[21,22,24] The best fit to the experimental magnetization data on $Tb_2@C_{79}N$ was obtained for $K = 45$ cm^{-1}, which places the states with antiparallel alignment of Tb-4f moments at 400–500 cm^{-1} (50–60 meV).[30] In the $Tb_2@C_{79}N$ anion, the last term in

eqn (1) vanishes, and the spin Hamiltonian is reduced to a simple form:

$$\hat{H}_{\text{spin}} = \hat{H}_{\text{LF}'} + \hat{H}_{\text{LF}''} - 2j_{12}\hat{J}_{\text{Tb}'}\hat{J}_{\text{Tb}''} + \hat{H}_{\text{ZEE}}. \quad (2)$$

In the first approximation, we assume that the ligand field terms for Tb ions in $Tb_2@C_{79}N$ and $Tb_2@C_{79}N^-$ are similar, which allows the use results of *ab initio* calculations from ref. 30 in further modelling. Since XMCD at the Tb-$M_{4,5}$ edge allows determination of Tb-4f moments only, we can use eqn (2) as an effective Hamiltonian for the neutral $Tb_2@C_{79}N$ as well. The correct energy of the $Tb_2@C_{79}N$ state with antiparallel alignment of Tb-4f moments is then obtained with the j_{12} constant of 4 cm^{-1}. Following *ab initio* predictions, the quantization axes of the two Tb ions in $Tb_2@C_{79}N$ are misaligned by 8°.

Fig. 10b shows simulated powder-averaged magnetization curves of $Tb_2@C_{79}N^-$ obtained with the Hamiltonian in eqn (2) and j_{12} values in the range of 0 to −0.4 cm^{-1} for T = 2 K. The shape of the curves with small magnetization at low field and fast increase above the threshold field corresponds well to the data measured for $Tb_2@C_{79}N$ adsorbed on Au(111). The j_{12} value of −0.25 cm^{-1} gives the zero-field energy difference between afm and fm-coupled states of 36 cm^{-1} (4.5 meV) and the threshold field of 4.1 T. For other substrates, the $Tb_2@C_{79}N^-$ anion alone with afm ground state cannot reproduce magnetization data, which is probably caused by a coexistence of $Tb_2@C_{79}N^-$ anion and neutral $Tb_2@C_{79}N$ molecules.

The coexistence of two types of species with different magnetic ground states can be further inferred from the temperature dependence of the Tb-4f magnetic moment, which was measured for $Tb_2@C_{79}N$ on MgO|Ag(100) substrate in the field of 6.8 T. Between 2 K and 15 K, the $\mu_{\text{Tb-4f}}$ value decreased slightly from 3.0 to 2.9μ_B, then increased to reach its maximum of 3.4μ_B at 35 K, and then showed gradual decrease at higher temperatures to the value of 0.7μ_B at 300 K (Fig. 10c). Note that the sum rule analysis gives the error up to 0.5μ_B due to uncertainty in integration limits and background, but the relative values of XMCD intensities are much more precise. We therefore determined the $\mu_{\text{Tb-4f}}$ value from the sum rule analysis at 35 K and estimated other points from their relative XMCD intensities at the Tb-M_5 edge.

The peak in the $\mu_{\text{Tb-4f}}(T)$ dependence is only possible with the afm state ($j_{12} < 0$) contribution because the fm ground state ($j_{12} > 0$) is characterized by a gradual decay of $\mu_{\text{Tb-4f}}$ in the whole temperature range. However, we cannot reproduce the shape of the $\mu_{\text{Tb-4f}}(T)$ curve with Hamiltonian (2) and any single j_{12} value. The peak in simulated $\mu_{\text{Tb-4f}}(T)$ curves develops only for j_{12} values more negative than −0.4 cm^{-1}, but simulated $\mu_{\text{Tb-4f}}$ values in the peak maximum are around 3 times smaller than experimental ones. At temperatures above 35 K, the experimental $\mu_{\text{Tb-4f}}$ is considerably larger than calculated for any negative j_{12}, but smaller than for j_{12} = 4 cm^{-1}. In fact, the part of the curve above 35 K can be reproduced by a combination of two species, neutral $Tb_2@C_{79}N$ with j_{12} of 4 cm^{-1} and $Tb_2@C_{79}N^-$ anion with j_{12} of −0.25 cm^{-1} in a 0.7 : 0.3 ratio (Fig. 10c). This ratio is only qualitatively estimated because of uncertainties of sum rule analysis, but the prevalence of the neutral $Tb_2@C_{79}N$ at higher temperatures is evident.

Thus, the shape of the $\mu_{\text{Tb-4f}}(T)$ curve with a peak at 35 K cannot be explained by any constant composition of the sample, and we suggest that the ratio between $Tb_2@C_{79}N^-$ and $Tb_2@C_{79}N$ is changing with temperature. If the anionic state is metastable, as it would be if it were formed by the electron trapping, its lifetime should depend on the rate of the electron hopping between neighboring molecules. In molecular solids, the hopping is often an activated process with a certain energy barrier. Thus, when the hopping is activated, the $Tb_2@C_{79}N^-$ fraction in the sample may decrease considerably, which would lead to the increase of the average magnetic moment and appearance of the peak in the $\mu_{\text{Tb-4f}}(T)$ curve.

Conclusions

In this work, we presented the first study of surface magnetism in lanthanide dimetallo-azafullerene monolayers on different substrates. In contrast to the single-molecule magnetism of the bulk $Tb_2@C_{79}N$ with strongly ferromagnetic intramolecular coupling, its monolayers showed unexpected antiferromagnetic coupling between Tb magnetic moments. The coupling is moderately strong, and the ferromagnetically-coupled state becomes prevalent in higher magnetic fields. The origin of the antiferromagnetic ground state in a monolayer is presumably the formation of $Tb_2@C_{79}N^-$ anions with two-fold occupied Tb–Tb bonding orbital. The anions can be formed either by an electron transfer from the substrate or, more likely, by trapping secondary electrons formed in the course of X-ray absorption measurements. The coexistence of neutral and anionic species exhibiting different magnetic properties and the variation of their ratio with temperature and as a function of the substrate result in unconventional magnetization behavior of $Tb_2@C_{79}N$ monolayers. On substrates with thin dielectric layers, h-BN|Rh(111) and MgO|Ag(100), we observed narrow magnetic hysteresis, presumably originating from the neutral $Tb_2@C_{79}N$ molecules.

Conflicts of interest

The authors declare no conflict of interest.

Acknowledgements

Computational resources were provided by ZIH/TU Dresden. The work was performed with financial support from Deutsche Forschungsgemeinschaft (grants PO 1602/7-1 and PO 1602/8-1 to A. A. P., LI 3055/3-1 to F. L., and AV 169/3-1 to S. M. A.), the Swedish Research Council (Grant No. 2015-00455), and Sklodowska Curie Actions cofounding project INCA 600398. We acknowledge the Paul Scherrer Institute for

providing synchrotron beamtime at the X-treme and PEARL beamlines of the Swiss Light Source.

References

1 A. A. Popov, S. Yang and L. Dunsch, *Chem. Rev.*, 2013, **113**, 5989–6113.
2 L. Spree and A. A. Popov, *Dalton Trans.*, 2019, **48**, 2861–2871.
3 T. Wang and C. Wang, *Small*, 2019, **15**, 1901522.
4 S. Yang, T. Wei and F. Jin, *Chem. Soc. Rev.*, 2017, **46**, 5005–5058.
5 X. Lu, W. Shen and S. Hu, *Chem. – Eur. J.*, 2020, **26**, 5748–5757.
6 A. A. Popov, *Endohedral Fullerenes: Electron Transfer and Spin*, Springer International Publishing, Cham, 2017.
7 W. Li, C.-R. Wang and T. Wang, *Chem. Commun.*, 2021, **57**, 10317–10326.
8 R. T. Harding, S. Zhou, J. Zhou, T. Lindvall, W. K. Myers, A. Ardavan, G. A. D. Briggs, K. Porfyrakis and E. A. Laird, *Phys. Rev. Lett.*, 2017, **119**, 140801.
9 J. E. Grose, E. S. Tam, C. Timm, M. Scheloske, B. Ulgut, J. J. Parks, H. D. Abruña, W. Harneit and D. C. Ralph, *Nat. Mater.*, 2008, **7**, 884–889.
10 *Endohedral Metallofullerenes: Basics and Applications*, ed. X. Lu, L. Echegoyen, A. L. Balch, S. Nagase and T. AkasakaCRC Press, 2014.
11 U. Reuther and A. Hirsch, *Carbon*, 2000, **38**, 1539–1549.
12 A. Hirsch and B. Nuber, *Acc. Chem. Res.*, 1999, **32**, 795–804.
13 J. C. Hummelen, B. Knight, J. Pavlovich, R. Gonzalez and F. Wudl, *Science*, 1995, **269**, 1554–1556.
14 T. Zuo, L. Xu, C. M. Beavers, M. M. Olmstead, W. Fu, T. D. Crawford, A. L. Balch and H. C. Dorn, *J. Am. Chem. Soc.*, 2008, **130**, 12992–12997.
15 K. Nakao, N. Kurita and M. Fujita, *Phys. Rev. B: Condens. Matter Mater. Phys.*, 1994, **49**, 11415–11420.
16 F. Liu, L. Spree, D. S. Krylov, G. Velkos, S. M. Avdoshenko and A. A. Popov, *Acc. Chem. Res.*, 2019, **52**, 2981–2993.
17 W. Fu, J. Zhang, T. Fuhrer, H. Champion, K. Furukawa, T. Kato, J. E. Mahaney, B. G. Burke, K. A. Williams, K. Walker, C. Dixon, J. Ge, C. Shu, K. Harich and H. C. Dorn, *J. Am. Chem. Soc.*, 2011, **133**, 9741–9750.
18 Z. Hu, B.-W. Dong, Z. Liu, J.-J. Liu, J. Su, C. Yu, J. Xiong, D.-E. Shi, Y. Wang, B.-W. Wang, A. Ardavan, Z. Shi, S.-D. Jiang and S. Gao, *J. Am. Chem. Soc.*, 2018, **140**, 1123–1130.
19 G. Velkos, D. S. Krylov, K. Kirkpatrick, X. Liu, L. Spree, A. U. B. Wolter, B. Buchner, H. C. Dorn and A. A. Popov, *Chem. Commun.*, 2018, **54**, 2902–2905.
20 X. Wang, J. E. McKay, B. Lama, J. van Tol, T. Li, K. Kirkpatrick, Z. Gan, S. Hill, J. R. Long and H. C. Dorn, *Chem. Commun.*, 2018, **54**, 2425–2428.
21 F. Cimpoesu, B. Frecus, C. I. Oprea, H. Ramanantoanina, W. Urland and C. Daul, *Mol. Phys.*, 2015, **113**, 1712–1727.
22 G. Rajaraman, M. K. Singh and N. Yadav, *Chem. Commun.*, 2015, **51**, 17732–17735.
23 F. Liu, G. Velkos, D. S. Krylov, L. Spree, M. Zalibera, R. Ray, N. A. Samoylova, C.-H. Chen, M. Rosenkranz, S. Schiemenz, F. Ziegs, K. Nenkov, A. Kostanyan, T. Greber, A. U. B. Wolter, M. Richter, B. Büchner, S. M. Avdoshenko and A. A. Popov, *Nat. Commun.*, 2019, **10**, 571.
24 F. Liu, D. S. Krylov, L. Spree, S. M. Avdoshenko, N. A. Samoylova, M. Rosenkranz, A. Kostanyan, T. Greber, A. U. B. Wolter, B. Büchner and A. A. Popov, *Nat. Commun.*, 2017, **8**, 16098.
25 Y. Wang, J. Xiong, J. Su, Z.-Q. Hu, F. Ma, R. Sun, X.-Y. Tan, H.-L. Sun, B. Wang, Z. Shi and S. Gao, *Nanoscale*, 2020, **12**, 11130–11135.
26 C. Zhao, H. Meng, M. Nie, Q. Huang, P. Du, C. Wang and T. Wang, *Chem. Commun.*, 2019, **55**, 11511–11514.
27 C. Zhao, H. Meng, M. Nie, L. Jiang, C. Wang and T. Wang, *J. Phys. Chem. C*, 2018, **122**, 4635–4640.
28 Y. Feng, T. Wang, Y. Li, J. Li, J. Wu, B. Wu, L. Jiang and C. Wang, *J. Am. Chem. Soc.*, 2015, **137**, 15055–15060.
29 R. B. Zaripov, Y. E. Kandrashkin, K. M. Salikhov, B. Büchner, F. Liu, M. Rosenkranz, A. A. Popov and V. Kataev, *Nanoscale*, 2020, **12**, 20513–20521.
30 G. Velkos, D. Krylov, K. Kirkpatrick, L. Spree, V. Dubrovin, B. Büchner, S. Avdoshenko, V. Bezmelnitsyn, S. Davis, P. Faust, J. Duchamp, H. Dorn and A. A. Popov, *Angew. Chem., Int. Ed.*, 2019, **58**, 5891–5896.
31 C. A. P. Goodwin, F. Ortu, D. Reta, N. F. Chilton and D. P. Mills, *Nature*, 2017, **548**, 439–442.
32 F.-S. Guo, B. M. Day, Y.-C. Chen, M.-L. Tong, A. Mansikkamäki and R. A. Layfield, *Science*, 2018, **362**, 1400–1403.
33 K. R. McClain, C. A. Gould, K. Chakarawet, S. Teat, T. J. Groshens, J. R. Long and B. G. Harvey, *Chem. Sci.*, 2018, **9**, 8492–8503.
34 C. Gould, K. R. McClain, J. Yu, T. J. Groshens, F. Furche, B. G. Harvey and J. R. Long, *J. Am. Chem. Soc.*, 2019, **141**, 12967–12973.
35 M. Mannini, F. Pineider, P. Sainctavit, C. Danieli, E. Otero, C. Sciancalepore, A. M. Talarico, M.-A. Arrio, A. Cornia, D. Gatteschi and R. Sessoli, *Nat. Mater.*, 2009, **8**, 194–197.
36 M. Mannini, F. Pineider, C. Danieli, F. Totti, L. Sorace, P. Sainctavit, M. A. Arrio, E. Otero, L. Joly, J. C. Cezar, A. Cornia and R. Sessoli, *Nature*, 2010, **468**, 417–421.
37 L. Malavolti, V. Lanzilotto, S. Ninova, L. Poggini, I. Cimatti, B. Cortigiani, L. Margheriti, D. Chiappe, E. Otero, P. Sainctavit, F. Totti, A. Cornia, M. Mannini and R. Sessoli, *Nano Lett.*, 2015, **15**, 535–541.
38 J.-P. Kappler, E. Otero, W. Li, L. Joly, G. Schmerber, B. Muller, F. Scheurer, F. Leduc, B. Gobaut, L. Poggini, G. Serrano, F. Choueikani, E. Lhotel, A. Cornia, R. Sessoli, M. Mannini, M.-A. Arrio, P. Sainctavit and P. Ohresser, *J. Synchrotron Radiat.*, 2018, **25**, 1727–1735.

39 G. Serrano, L. Poggini, M. Briganti, A. L. Sorrentino, G. Cucinotta, L. Malavolti, B. Cortigiani, E. Otero, P. Sainctavit, S. Loth, F. Parenti, A.-L. Barra, A. Vindigni, A. Cornia, F. Totti, M. Mannini and R. Sessoli, *Nat. Mater.*, 2020, **19**, 546–551.

40 L. Margheriti, D. Chiappe, M. Mannini, P. E. Car, P. Sainctavit, M.-A. Arrio, F. B. de Mongeot, J. C. Cezar, F. M. Piras, A. Magnani, E. Otero, A. Caneschi and R. Sessoli, *Adv. Mater.*, 2010, **22**, 5488–5493.

41 M. Gonidec, R. Biagi, V. Corradini, F. Moro, V. De Renzi, U. del Pennino, D. Summa, L. Muccioli, C. Zannoni, D. B. Amabilino and J. Veciana, *J. Am. Chem. Soc.*, 2011, **133**, 6603–6612.

42 A. Lodi Rizzini, C. Krull, T. Balashov, A. Mugarza, C. Nistor, F. Yakhou, V. Sessi, S. Klyatskaya, M. Ruben, S. Stepanow and P. Gambardella, *Nano Lett.*, 2012, **12**, 5703–5707.

43 M. Mannini, F. Bertani, C. Tudisco, L. Malavolti, L. Poggini, K. Misztal, D. Menozzi, A. Motta, E. Otero, P. Ohresser, P. Sainctavit, G. G. Condorelli, E. Dalcanale and R. Sessoli, *Nat. Commun.*, 2014, **5**, 4582.

44 D. Klar, A. Candini, L. Joly, S. Klyatskaya, B. Krumme, P. Ohresser, J.-P. Kappler, M. Ruben and H. Wende, *Dalton Trans.*, 2014, **43**, 10686–10689.

45 C. Nistor, C. Krull, A. Mugarza, S. Stepanow, C. Stamm, M. Soares, S. Klyatskaya, M. Ruben and P. Gambardella, *Phys. Rev. B: Condens. Matter Mater. Phys.*, 2015, **92**, 184402.

46 C. Wäckerlin, F. Donati, A. Singha, R. Baltic, S. Rusponi, K. Diller, F. Patthey, M. Pivetta, Y. Lan, S. Klyatskaya, M. Ruben, H. Brune and J. Dreiser, *Adv. Mater.*, 2016, **28**, 5195–5199.

47 G. Cucinotta, L. Poggini, A. Pedrini, F. Bertani, N. Cristiani, M. Torelli, P. Graziosi, I. Cimatti, B. Cortigiani, E. Otero, P. Ohresser, P. Sainctavit, A. Dediu, E. Dalcanale, R. Sessoli and M. Mannini, *Adv. Funct. Mater.*, 2017, **27**, 1703600.

48 A. Pedrini, L. Poggini, C. Tudisco, M. Torelli, A. E. Giuffrida, F. Bertani, I. Cimatti, E. Otero, P. Ohresser, P. Sainctavit, M. Suman, G. G. Condorelli, M. Mannini and E. Dalcanale, *Small*, 2018, **14**, 1702572.

49 G. Serrano, E. Velez-Fort, I. Cimatti, B. Cortigiani, L. Malavolti, D. Betto, A. Ouerghi, N. B. Brookes, M. Mannini and R. Sessoli, *Nanoscale*, 2018, **10**, 2715–2720.

50 K. Diller, A. Singha, M. Pivetta, C. Wäckerlin, R. Hellwig, A. Verdini, A. Cossaro, L. Floreano, E. Vélez-Fort, J. Dreiser, S. Rusponi and H. Brune, *RSC Adv.*, 2019, **9**, 34421–34429.

51 M. Studniarek, C. Wäckerlin, A. Singha, R. Baltic, K. Diller, F. Donati, S. Rusponi, H. Brune, Y. Lan, S. Klyatskaya, M. Ruben, A. P. Seitsonen and J. Dreiser, *Adv. Sci.*, 2019, **6**, 1901736.

52 Y. Lan, S. Klyatskaya, M. Ruben, O. Fuhr, W. Wernsdorfer, A. Candini, V. Corradini, A. Lodi Rizzini, U. del Pennino, F. Troiani, L. Joly, D. Klar, H. Wende and M. Affronte, *J. Mater. Chem. C*, 2015, **3**, 9794–9801.

53 M. D. Korzyński, Z. J. Berkson, B. Le Guennic, O. Cador and C. Copéret, *J. Am. Chem. Soc.*, 2021, **143**, 5438–5444.

54 A. Cornia, M. Mannini, R. Sessoli and D. Gatteschi, *Eur. J. Inorg. Chem.*, 2019, 552–568.

55 L. Poggini, E. Tancini, C. Danieli, A. L. Sorrentino, G. Serrano, A. Lunghi, L. Malavolti, G. Cucinotta, A.-L. Barra, A. Juhin, M.-A. Arrio, W. Li, E. Otero, P. Ohresser, L. Joly, J. P. Kappler, F. Totti, P. Sainctavit, A. Caneschi, R. Sessoli, A. Cornia and M. Mannini, *Adv. Mater. Interfaces*, 2021, **8**, 2101182.

56 C.-H. Chen, L. Spree, E. Koutsouflakis, D. S. Krylov, F. Liu, A. Brandenburg, G. Velkos, S. Schimmel, S. M. Avdoshenko, A. Fedorov, E. Weschke, F. Choueikani, P. Ohresser, J. Dreiser, B. Büchner and A. A. Popov, *Adv. Sci.*, 2021, **8**, 2000777.

57 D. S. Krylov, S. Schimmel, V. Dubrovin, F. Liu, T. T. N. Nguyen, L. Spree, C.-H. Chen, G. Velkos, C. Bulbucan, R. Westerström, M. Studniarek, J. Dreiser, C. Hess, B. Büchner, S. M. Avdoshenko and A. A. Popov, *Angew. Chem., Int. Ed.*, 2020, **59**, 5756–5764.

58 T. Greber, A. P. Seitsonen, A. Hemmi, J. Dreiser, R. Stania, F. Matsui, M. Muntwiler, A. A. Popov and R. Westerström, *Phys. Rev. Mater.*, 2019, **3**, 014409.

59 C. H. Chen, D. S. Krylov, S. M. Avdoshenko, F. Liu, L. Spree, R. Westerström, C. Bulbucan, M. Studniarek, J. Dreiser, A. U. B. Wolter, B. Büchner and A. A. Popov, *Nanoscale*, 2018, **10**, 11287–11292.

60 R. Westerström, A.-C. Uldry, R. Stania, J. Dreiser, C. Piamonteze, M. Muntwiler, F. Matsui, S. Rusponi, H. Brune, S. Yang, A. Popov, B. Büchner, B. Delley and T. Greber, *Phys. Rev. Lett.*, 2015, **114**, 087201.

61 F. Paschke, T. Birk, V. Enenkel, F. Liu, V. Romankov, J. Dreiser, A. A. Popov and M. Fonin, *Adv. Mater.*, 2021, **33**, 2102844.

62 L. Spree, F. Liu, V. Neu, M. Rosenkranz, G. Velkos, Y. Wang, S. Schiemenz, J. Dreiser, P. Gargiani, M. Valvidares, C.-H. Chen, B. Büchner, S. M. Avdoshenko and A. A. Popov, *Adv. Funct. Mater.*, 2021, **31**, 2105516.

63 A. Hemmi, C. Bernard, H. Cun, S. Roth, M. Klöckner, T. Kälin, M. Weinl, S. Gsell, M. Schreck, J. Osterwalder and T. Greber, *Rev. Sci. Instrum.*, 2014, **85**, 035101.

64 M. Corso, W. Auwärter, M. Muntwiler, A. Tamai, T. Greber and J. Osterwalder, *Science*, 2004, **303**, 217–220.

65 M. Muntwiler, J. Zhang, R. Stania, F. Matsui, P. Oberta, U. Flechsig, L. Patthey, C. Quitmann, T. Glatzel, R. Widmer, E. Meyer, T. A. Jung, P. Aebi, R. Fasel and T. Greber, *J. Synchrotron Radiat.*, 2017, **24**, 354–366.

66 C. Piamonteze, U. Flechsig, S. Rusponi, J. Dreiser, J. Heidler, M. Schmidt, R. Wetter, M. Calvi, T. Schmidt, H. Pruchova, J. Krempasky, C. Quitmann, H. Brune and F. Nolting, *J. Synchrotron Radiat.*, 2012, **19**, 661–674.

67 J. Hafner, *J. Comput. Chem.*, 2008, **29**, 2044–2078.

68 G. Kresse and J. Hafner, *Phys. Rev. B: Condens. Matter Mater. Phys.*, 1993, **47**, 558–561.

69 G. Kresse and D. Joubert, *Phys. Rev. B: Condens. Matter Mater. Phys.*, 1999, **59**, 1758–1775.
70 J. P. Perdew, K. Burke and M. Ernzerhof, *Phys. Rev. Lett.*, 1996, **77**, 3865–3868.
71 S. Grimme, *Wiley Interdiscip. Rev.: Comput. Mol. Sci.*, 2011, **1**, 211–228.
72 G. Henkelman, A. Arnaldsson and H. Jónsson, *Comput. Mater. Sci.*, 2006, **36**, 354–360.
73 N. F. Chilton, R. P. Anderson, L. D. Turner, A. Soncini and K. S. Murray, *J. Comput. Chem.*, 2013, **34**, 1164–1175.
74 T. Sakurai, X. D. Wang, Q. K. Xue, Y. Hasegawa, T. Hashizume and H. Shinohara, *Prog. Surf. Sci.*, 1996, **51**, 263–408.
75 N. Neel, J. Kroger and R. Berndt, *Appl. Phys. Lett.*, 2006, **88**, 163101.
76 M. Grobis, A. Wachowiak, R. Yamachika and M. F. Crommie, *Appl. Phys. Lett.*, 2005, **86**, 204102.
77 I. Fernández Torrente, K. J. Franke and J. Ignacio Pascual, *J. Phys.: Condens. Matter*, 2008, **20**, 184001.
78 S. Vijayaraghavan, D. Écija, W. Auwärter, S. Joshi, K. Seufert, A. P. Seitsonen, K. Tashiro and J. V. Barth, *Nano Lett.*, 2012, **12**, 4077–4083.
79 M. Jung, D. Shin, S.-D. Sohn, S.-Y. Kwon, N. Park and H.-J. Shin, *Nanoscale*, 2014, **6**, 11835–11840.
80 D. R. Daughton and J. A. Gupta, *Appl. Phys. Lett.*, 2011, **98**, 133303.
81 T. Susi, T. Pichler and P. Ayala, *Beilstein J. Nanotechnol.*, 2015, **6**, 177–192.
82 K. Schulte, L. Wang, P. J. Moriarty, K. Prassides and N. Tagmatarchis, *J. Chem. Phys.*, 2007, **126**, 184707.
83 S. Hino, M. Zenki, T. Zaima, Y. Aoki, S. Okita, T. Ohta, H. Yagi, T. Miyazaki, R. Sumii, H. Okimoto, Y. Ito and H. Shinohara, *J. Phys. Chem. C*, 2012, **116**, 165–170.
84 L. Alvarez, T. Pichler, P. Georgi, T. Schwieger, H. Peisert, L. Dunsch, Z. Hu, M. Knupfer, J. Fink, P. Bressler, M. Mast and M. S. Golden, *Phys. Rev. B: Condens. Matter Mater. Phys.*, 2002, **66**, 035107.
85 R. Stania, A. P. Seitsonen, D. Kunhardt, B. Büchner, A. A. Popov, M. Muntwiler and T. Greber, *J. Phys. Chem. Lett.*, 2018, **9**, 3586–3590.
86 J. A. Leiro, M. H. Heinonen, T. Laiho and I. G. Batirev, *J. Electron Spectrosc. Relat. Phenom.*, 2003, **128**, 205–213.
87 A. Goldoni, C. Cepek, R. Larciprete, L. Sangaletti, S. Pagliara, G. Paolucci and M. Sancrotti, *Phys. Rev. Lett.*, 2002, **88**, 196102.
88 X. Liu, M. Krause, J. Wong, T. Pichler, L. Dunsch and M. Knupfer, *Phys. Rev. B: Condens. Matter Mater. Phys.*, 2005, **72**, 085407.
89 H. Shiozawa, H. Rauf, T. Pichler, D. Grimm, X. Liu, M. Knupfer, M. Kalbac, S. Yang, L. Dunsch, B. Buchner and D. Batchelor, *Phys. Rev. B: Condens. Matter Mater. Phys.*, 2005, **72**, 195409.
90 E. Magnano, S. Vandre, C. Cepek, A. Goldoni, A. D. Laine, G. M. Curro, A. Santaniello and M. Sancrotti, *Surf. Sci.*, 1997, **377**, 1066–1070.
91 F. Gerken, *J. Phys. F: Met. Phys.*, 1983, **13**, 703–713.
92 M. Krause, X. J. Liu, J. Wong, T. Pichler, M. Knupfer and L. Dunsch, *J. Phys. Chem. A*, 2005, **109**, 7088–7093.
93 T. Pichler, M. S. Golden, M. Knupfer, J. Fink, U. Kirbach, P. Kuran and L. Dunsch, *Phys. Rev. Lett.*, 1997, **79**, 3026–3029.
94 V. Dubrovin, L.-H. Gan, B. Büchner, A. A. Popov and S. M. Avdoshenko, *Phys. Chem. Chem. Phys.*, 2019, **21**, 8197–8200.
95 E. Sanville, S. D. Kenny, R. Smith and G. Henkelman, *J. Comput. Chem.*, 2007, **28**, 899–908.
96 J. Dreiser, R. Westerström, C. Piamonteze, F. Nolting, S. Rusponi, H. Brune, S. Yang, A. Popov, L. Dunsch and T. Greber, *Appl. Phys. Lett.*, 2014, **105**, 032411.
97 F. Paschke, T. Birk, S. M. Avdoshenko, F. Liu, A. A. Popov and M. Fonin, *Small*, 2022, **18**, 2105667.
98 G. Pacchioni and H. Freund, *Chem. Rev.*, 2013, **113**, 4035–4072.
99 M. Hollerer, D. Lüftner, P. Hurdax, T. Ules, S. Soubatch, F. S. Tautz, G. Koller, P. Puschnig, M. Sterrer and M. G. Ramsey, *ACS Nano*, 2017, **11**, 6252–6260.
100 P. Hurdax, M. Hollerer, P. Puschnig, D. Lüftner, L. Egger, M. G. Ramsey and M. Sterrer, *Adv. Mater. Interfaces*, 2020, **7**, 2000592.
101 L. Egger, M. Hollerer, C. S. Kern, H. Herrmann, P. Hurdax, A. Haags, X. Yang, A. Gottwald, M. Richter, S. Soubatch, F. S. Tautz, G. Koller, P. Puschnig, M. G. Ramsey and M. Sterrer, *Angew. Chem., Int. Ed.*, 2021, **60**, 5078–5082.
102 P. Hurdax, M. Hollerer, L. Egger, G. Koller, X. Yang, A. Haags, S. Soubatch, F. S. Tautz, M. Richter, A. Gottwald, P. Puschnig, M. Sterrer and M. G. Ramsey, *Beilstein J. Nanotechnol.*, 2020, **11**, 1492–1503.
103 A. Singha, D. Sostina, C. Wolf, S. L. Ahmed, D. Krylov, L. Colazzo, P. Gargiani, S. Agrestini, W.-S. Noh, J.-H. Park, M. Pivetta, S. Rusponi, H. Brune, A. J. Heinrich, A. Barla and F. Donati, *ACS Nano*, 2021, **15**, 16162–16171.
104 F. Donati, M. Pivetta, C. Wolf, A. Singha, C. Wäckerlin, R. Baltic, E. Fernandes, J.-G. de Groot, S. L. Ahmed, L. Persichetti, C. Nistor, J. Dreiser, A. Barla, P. Gambardella, H. Brune and S. Rusponi, *Nano Lett.*, 2021, **21**, 8266–8273.
105 W. Auwärter, *Surf. Sci. Rep.*, 2019, **74**, 1–95.
106 M. Muntwiler, W. Auwärter, A. P. Seitsonen, J. Osterwalder and T. Greber, *Phys. Rev. B: Condens. Matter Mater. Phys.*, 2005, **71**, 121402.
107 D. Vlachos, A. J. Craven and D. W. McComb, *J. Synchrotron Radiat.*, 2005, **12**, 224–233.
108 A. Cros, *J. Electron Spectrosc. Relat. Phenom.*, 1992, **59**, 1–14.
109 J. Cazaux, *J. Electron Spectrosc. Relat. Phenom.*, 1999, **105**, 155–185.
110 M. A. Ruderman and C. Kittel, *Phys. Rev.*, 1954, **96**, 99–102.
111 T. Kasuya, *Prog. Theor. Phys.*, 1956, **16**, 45–57.
112 K. Yosida, *Phys. Rev.*, 1957, **106**, 893–898.